nature chemistry

Article

https://doi.org/10.1038/s41557-025-01911-y

Nucleation processes at interfaces with both substrate and electrolyte control lithium growth

Received: 26 July 2024

Accepted: 15 July 2025

Published online: 14 August 2025



Check for updates

Zeyu Hui^{1,3}, Sicen Yu^{2,3}, Shen Wang 1, Gayea Hyun¹, John Holoubek 1, Ke Zhou¹, Jenny Nicolas © ², Mengchen Liu¹, Qiushi Miao², Shuangjie Tan © ¹, Victoria Petrova², Haichen Lin², Jianbin Zhou¹, Haodong Liu¹ & Ping Liu 10 1.2 2.2

Understanding the lithium nucleation and growth process is crucial for improving lithium metal battery performance. Here we investigate the roles of the lithium-electrolyte and lithium-substrate interfaces during the lithium nucleation process. Using a physics-based model, we identify which of the two interfaces controls lithium nucleation for different electrolytes and substrates. Sluggish lithium transport through the solid-electrolyte interphases (SEIs) and slow charge-transfer kinetics make the nucleation process SEI controlled and substrate independent, while substrate properties control lithium nucleation in a system having fast SEI transport and charge-transfer reactions. For substrate-controlled nucleation, we derive a model that elucidates the need for fast lithium adatom velocity along the substrate that outpaces the critical nuclei formation. We also reveal that lithium nucleation modes have a strong impact on lithium plating/stripping reversibility. Simultaneous fast transport through the SEIs and fast lithium adatom movement on the substrate are essential for achieving dense lithium deposition and long-cycle-life lithium metal batteries.

The reversible cycling of lithium-metal anodes holds the key to realizing high-energy-density batteries¹. However, uncontrolled lithium deposition and irreversible stripping leads to poor cyclability and increased safety hazards²⁻⁵. As the initial step of lithium deposition, the nucleation morphology significantly impacts the final morphology of deposited lithium^{6,7}. Controlling the lithium nucleation process is thus crucial for enabling the stable cycling of lithium-metal anodes⁸⁻¹⁰.

It is generally accepted that two interfaces, lithium-substrate and lithium-electrolyte (the latter involving solid-electrolyte interphases (SEIs)), play a critical role in controlling lithium nucleation and determining subsequent lithium growth morphology¹¹⁻¹⁴. Substrates impact the thermodynamic lithium nucleation barrier (overpotential) by having different affinities for lithium metal¹⁵. Lithium nucleation preferentially takes place on those sites with lower energy barriers. As a result, various substrates have been developed with the aim of reducing the lithium nucleation barrier, including metal-based substrates such as gold and magnesium that form alloys with lithium¹⁵⁻¹⁷, doped-carbon substrates¹⁷⁻¹⁹ and other three-dimensional hosts^{20–22}. The migration barrier for lithium on the substrate's surface is another important factor for lithium nucleation regulation²³. Density functional theory (DFT) calculations show that compared with other species such as Li₂O and Li₂CO₃, lithium halides exhibit higher surface energies and lower surface diffusion barriers²⁴, which facilitate the surface migration of lithium. This theory is corroborated by the discovery of a nanocomposite substrate containing metal nanoparticles as uniform nucleation sites and lithium fluoride (LiF) which facilitates surface migration. The substrate was found to enable uniform single-crystalline lithium nucleation despite its apparent lithiophobility²⁵. Overall, the design of substrates has been mainly driven by the desire to enhance affinity between lithium and the substrate to reduce nucleation energy, with a more recent consideration being lithium surface mobility.

¹Aiiso Yufeng Li Family Department of Nanoengineering, University of California, San Diego, La Jolla, CA, USA. ²Program of Material Science, University of California, San Diego, La Jolla, CA, USA. 3These authors contributed equally: Zeyu Hui, Sicen Yu. 🖂 e-mail: piliu@ucsd.edu

The lithium-electrolyte interface (SEI) also plays a crucial role in determining lithium nucleation morphology. Recent studies²⁶⁻²⁸ revealed that when lithium is deposited under ultrahigh current density and lithium nucleation is allowed to outpace the formation of the SEI, lithium forms single-crystalline rhombic dodecahedra, regardless of the plating substrate or electrolyte chemistry. However, when lithium is deposited in the presence of an existing SEI (under practical operating conditions), the morphology of lithium nucleation and early growth is highly dependent on the SEI composition and morphology, which is dictated by the electrolyte chemistry. With an SEI that allows facile lithium diffusion, lithium atoms can rearrange and effectively release local stress, which helps avoid SEI breakage and dendrite extrusion, thus enabling uniform and planar (two-dimensional) lithium nucleation and growth²⁹. This has driven the approach to generate SEIs rich in LiF, which is known to enable fast lithium transport inside SEIs^{29–32}. Additionally, SEIs with high lithium ion conductivity³³, improved uniformity³, robustness and flexibility^{34,35} serve the same purpose of suppressing SEI breakage^{36,37}.

Experimental and theoretical investigations thus far have provided in-depth understanding on the role that each interface plays during lithium nucleation. However, under practical battery operating conditions, the two interfaces always coexist, that is, lithium is expected to nucleate and grow between the substrate and an SEI that has already formed. Consequently, it is essential to understand which interface will play the deciding role in the lithium nucleation under a given substrate, electrolyte and other experimental conditions. Furthermore, such consideration needs to be extended to the subsequent growth, that is, whether the lithium interface with predeposited lithium nuclei or whether the lithium interface with the electrolyte (SEI) will determine the growth behaviour. By understanding which interface dictates nucleation and growth behaviour, the necessary design principles can be used to optimize battery performance.

In this study, we use quantitative models to elucidate the limiting interfaces for lithium nucleation in batteries with different substrates and SEI chemistries. By carrying out the study at room temperature and using practical deposition current densities (with the existence of an SEI), we find that the lithium nucleation process can be either substrate controlled or SEI controlled (substrate independent), which is determined by the electrolyte and SEI chemistries. Although both cases can generate dendrite-free lithium growth, SEI-controlled lithium nucleation can be harmful to cycling stability, regardless of the choice of substrate for lithium deposition. In the SEI-controlled process. nucleation is continuous during the growth process. The resulting nucleation-driven multilayer growth mode leads to weak connections between lithium particles and promotes dead lithium formation upon stripping, which is detrimental to cycling reversibility and stability. In contrast, a substrate-driven nucleation process, particularly one that features rapid lithium transport at the lithium-substrate interface, leads to uniform faceted lithium seeds followed by an extrusion-based growth process. The deposited lithium particles have better connectivity, thus suppressing the formation of isolated dead lithium. The insights from this study will facilitate the design of new electrolytes and substrates to further advance the cycling stability of lithium-metal batteries.

Results and discussion

A study matrix to probe the effect of substrate and SEIs on lithium nucleation

We first construct a matrix of two substrates and four electrolytes to probe the effect of lithium–substrate and lithium–electrolyte interfaces on lithium nucleation and early growth. In addition to commonly used copper substrate, we also tested a Ni/LiF nanocomposite substrate. Previously, we have shown that a metal/LiF nanocomposite substrate enables uniform single-crystalline lithium nucleation 25 . In our case, a thin film of NiF $_2$ is deposited on copper by thermal evaporation. The film is then lithiated electrochemically in situ to form a nanocomposite

of nickel and LiF. As described in Supplementary Section 3, chemical and morphological characterization results (Supplementary Figs. 1–8) show that the Ni/LiF substrate has uniform composition, morphology and electronic conductivity.

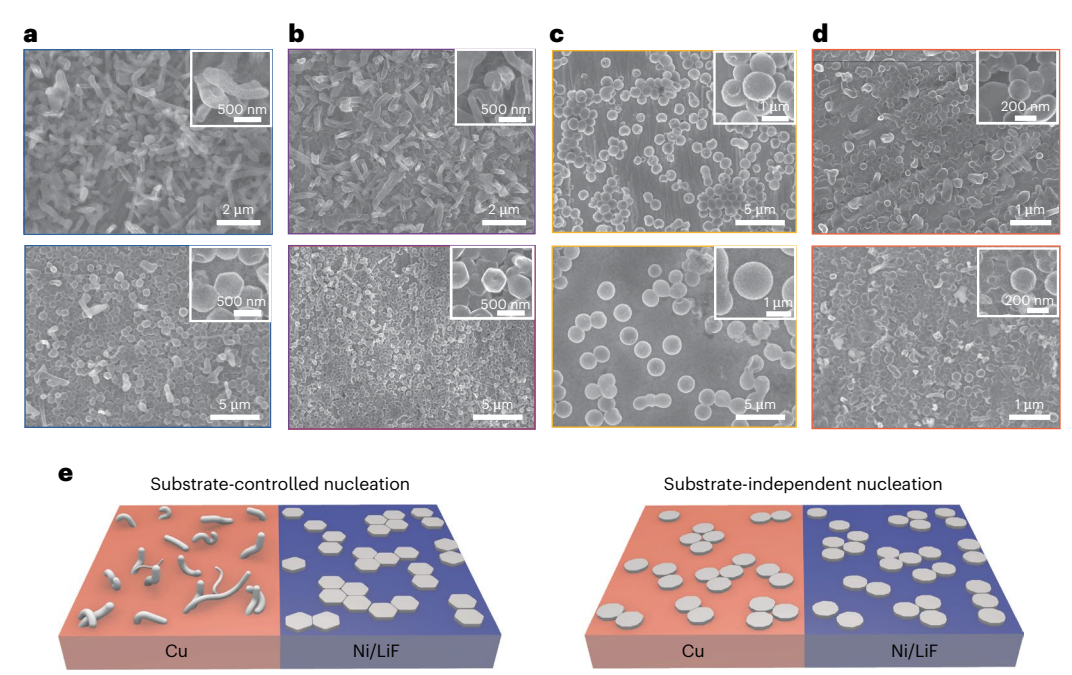
To investigate the effect of the SEIs, we select four electrolyte systems to cover the commonly used electrolyte types: (1) a localized high-concentration electrolyte (LDME)³⁸: 2 M lithium bis(fluorosulfonyl) imide (LiFSI) in 1,2-dimethoxyethane (DME) + bis(2,2,2-trifluoroethyl) ether (BTFE), which is well known to offer high-efficiency lithium cycling; (2) an all-fluorinated carbonate electrolyte (All F)³⁹: 1 M LiPF₆ in fluoroethylene carbonate (FEC) + 1,1,2,2-tetrafluoroethyl 2,2,3,3-tetrafluoropropyl ether (TTE) + methyl (2,2,2-trifluoroethyl) carbonate (FEMC), also reported to offer high-efficiency and dendrite-free cycling: (3) a dilute ether electrolyte with LiNO₃ additive (DOLDME)⁷: 1 M lithium bis(trifluoromethanesulfonyl)imide (LiTFSI) in 1,3-dioxolane (DOL) + DME + 1% LiNO₃, which is most commonly used for lithium-sulfur batteries; and (4) a fluorine-free carbonate electrolyte (F-Free): 1 M lithium bis(oxalato)borate (LiBOB) in ethylene carbonate (EC) + dimethyl carbonate (DMC), which is chosen to exclude the formation of Lif. Figure 1 shows the resulting lithium nucleation morphology as a function of substrate and electrolyte (SEI). Lithium is deposited at a current density of 3 mA cm⁻² and a capacity of 0.1 mAh cm⁻². In the LDME and All F electrolytes (Fig. 1a,b), lithium nucleation is strongly affected by the specific substrate. Whereas the Ni/LiF substrate enables uniform single-crystalline lithium nucleation, lithium deposited on copper appears as irregular dendrites. Supplementary Fig. 9 shows the uniform single-crystalline lithium nucleation at larger length scales (100-µm scale and millimetre scale) on the Ni/LiF substrate, again confirming its uniformity. In contrast, the DOLDME and F-Free electrolytes (Fig. 1c,d) enable uniform dendrite-free lithium nucleation on both copper and the nanocomposite substrate. Thus, the study matrix allows us to categorize the lithium nucleation into two modes: substrate-controlled nucleation versus substrate-independent nucleation (Fig. 1e). Supplementary Figs. 10 and 11 show the voltage profiles for lithium nucleation. Noticeably, the F-Free electrolyte shows much higher polarization than the other three electrolytes. However, these profiles do not otherwise provide any information that would indicate the different nucleation modes.

Unveiling the limiting interface during nucleation

To unveil the limiting interface for lithium nucleation, we adopt a physics-based model to describe the lithium nucleation phenomena. To ensure an analysis with high accuracy, here we only apply the quantitative analysis based on the model to the lithium nucleation on the Ni/LiF nanocomposite substrate because this promotes lithium nucleation with uniform size and regular shape for all electrolytes under different applied current densities. At the stage of lithium nucleation on the Ni/LiF substrate, the source of overpotential can be expressed by four components (illustrated in Supplementary Fig. 12; lithium movement on predeposited lithium surface is ignored at this early stage), which are sequentially shown in equation (1): (1) transport of lithium through the bulk electrolyte and the thickness of the SEI; (2) transport of lithium adatoms along the active surface; (3) Li/Li+ charge-transfer kinetics and (4) interfacial energy of critical lithium nuclei formation 40 .

$$\eta = \frac{irRT}{D_1c_1F^2} + \frac{ir^2RT}{D_2c_2F^2} + \frac{RT}{\alpha F} \ln \frac{i}{i_0} + \frac{2\gamma V_{Li}}{Fr}$$
 (1)

Here, η is the lithium nucleation overpotential (V), i is the effective current density (mA cm⁻²), i_0 is the exchange current density (mA cm⁻²), r is the lithium nucleation size (cm), D_1 and D_2 are the effective lithium diffusion coefficients for through-plane and in-plane directions, respectively (cm² s⁻¹), c_1 is the bulk/SEI lithium ion concentration (mol cm⁻³), c_2 is the surface lithium concentration (mol cm⁻²), γ is the



 $\label{lem:fig.1} Fig. 1 | Effect of substrate and electrolyte on lithium nucleation morphology to probe the roles of the lithium–substrate and lithium–electrolyte (SEI) interfaces. a–d, Lithium deposited on copper substrate (top) and on Ni/LiF nanocomposite substrate (bottom), in LDME electrolyte (a), All F electrolyte (b), \\$

DOLDME electrolyte (\mathbf{c}) and F-Free electrolyte (\mathbf{d}). Current density, 3 mA cm $^{-2}$; deposited capacity, 0.1 mAh cm $^{-2}$. \mathbf{e} , Schematic illustrations of two lithium nucleation modes; substrate controlled and substrate independent.

interfacial energy (J cm $^{-2}$), $V_{\rm Li}$ is the molar volume of lithium (cm 3 mol $^{-1}$), α is the charge-transfer coefficient, R is the gas constant (J mol $^{-1}$ K $^{-1}$), F is Faraday's constant (C mol $^{-1}$) and T is the temperature (K). In this model, we neglect the effect of convection and concentration polarization. Detailed explanations are provided in Supplementary Section 4. In particular, we developed a continuum-level porous electrode model (Supplementary Table 1) to quantify the effect of concentration polarization. As shown in Supplementary Fig. 13, during the lithium nucleation stage, the overpotential contribution from the ion concentration gradient is \sim 6 mV, which is negligible compared with the total lithium nucleation overpotential (>200 mV). This is to be expected since the time scale for nucleation (\sim 10 s) very different from the Sand's time. Our treatment is consistent with previous reports⁴⁰.

Considering the non-perfect surface coverage of lithium nuclei in the initial nucleation stage, the applied surface current density $(i_{\rm applied})$ is correlated with the effective current density (i) by a surface coverage factor (θ) :

$$i = i_{\text{applied}}/\theta \tag{2}$$

To determine the value for θ , we analysed scanning electron microscopy (SEM) images of lithium deposited at the very initial stage of nucleation (0.01 mAh cm⁻²) under different current densities (Supplementary Figs. 14–17) by measuring the nuclei size and number density. This stage of lithium nucleation (0.01 mAh cm⁻²) is chosen to reflect the surface coverage at the start of nucleation (Supplementary Fig. 18). This offers a quantitative correlation between surface coverage and nuclei size:

$$\theta \approx r^{-x} \tag{3}$$

where the exponent coefficient *x* is fitted from image-analysis data (Supplementary Figs. 14–17). Equation (1) can be converted into:

$$\eta = \frac{\beta i_{\text{applied}} r^{1+x} RT}{D_1 c_1 F^2} + \frac{\beta i_{\text{applied}} r^{2+x} RT}{D_2 c_2 F^2} + \frac{RT}{\alpha F} \ln \frac{\beta i_{\text{applied}} r^x}{i_0} + \frac{2\gamma V_{\text{Li}}}{Fr}$$
(4)

where β is the constant to match the dimension (cm^{-x}). To determine the nuclei size that leads to the lowest nucleation overpotential and is most energetically stable, we minimize the lithium nucleation overpotential with respect to nuclei size:

$$\frac{\partial \eta}{\partial r} = 0 \tag{5}$$

Combining equations (4) and (5), we obtain the following:

$$i_{\text{applied}} = \frac{\frac{2\gamma V_{\text{Li}}}{F} - \frac{xRT}{\alpha F} r}{\beta \frac{(1+x)RT}{D_1 C_1 F^2} r^{2+x} + \beta \frac{(2+x)RT}{D_2 C_2 F^2} r^{3+x}}$$
(6)

Equation (6) establishes the correlation between two experimentally measurable variables: applied current density ($i_{applied}$) and lithium nuclei size (r). Moreover, the right-hand side expression preserves the four terms corresponding to the four sources of lithium nucleation overpotential, with each term having a different order of dependence on r. This enables direct application of the model to the experimental observations (Supplementary Fig. 19). For example, if the lithium nucleation process is limited by the substrate surface properties (that is, by the interfacial energy and/or by the lithium surface transport), then the equation can be reduced to:

$$i_{\text{applied}} = \frac{\frac{2\gamma V_{\text{Li}}}{F}}{\beta \frac{(2+x)RT}{D_2 C_2 F^2} r^{3+x}} = \frac{2\gamma V_{\text{Li}} D_2 C_2 F}{\beta (2+x)RT} r^{-(3+x)}$$
(7)

Whereas if the SEI property controls the lithium nucleation process by limiting the lithium through-plane transport and/or by limiting the charge transfer, the equation can be reduced to:

$$i_{\text{applied}} = \frac{\frac{xRT}{\alpha F}r}{\beta \frac{(1+x)RT}{D_1C_1F^2}r^{2+x}} = \frac{xD_1C_1F}{\beta \alpha (1+x)}r^{-(1+x)}$$
(8)

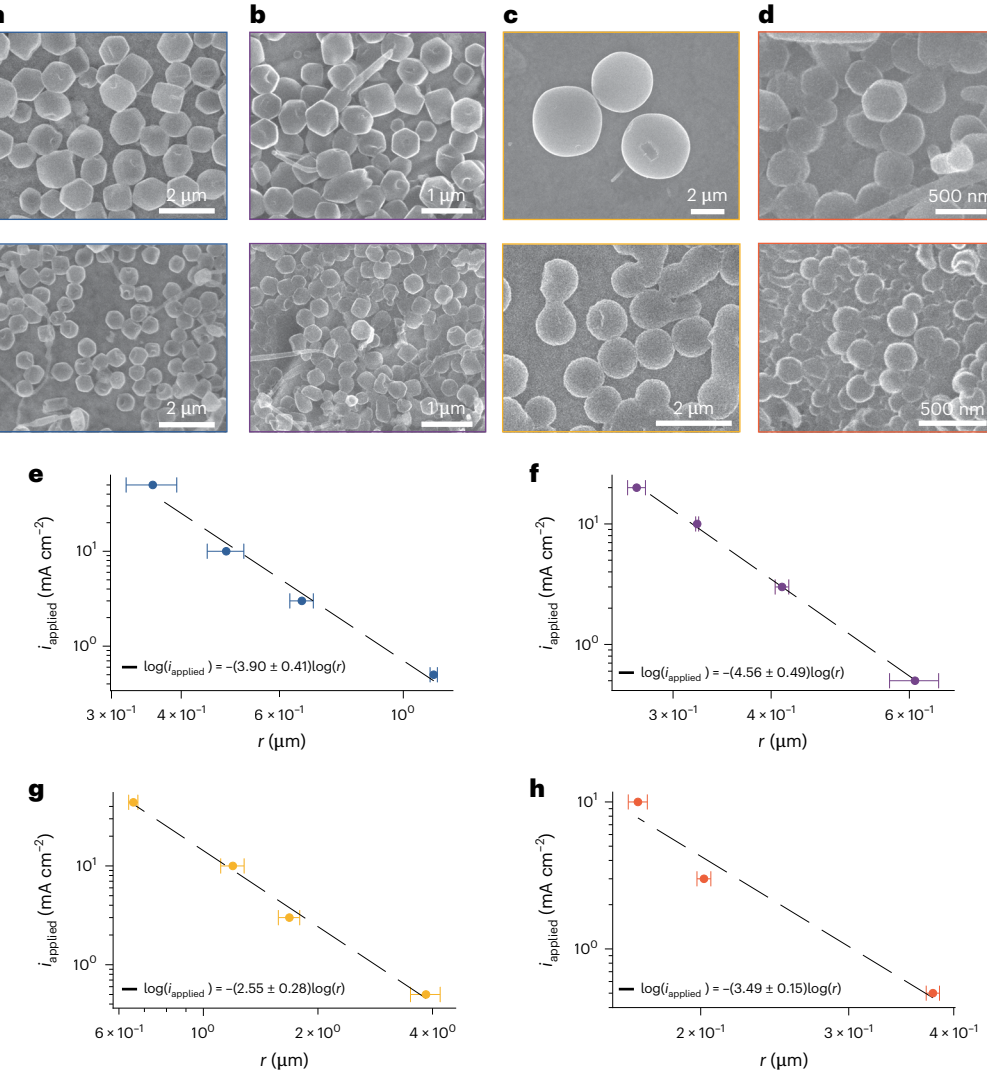


Fig. 2 | The nuclei size–current density relationship as a function of electrolyte chemistry. \mathbf{a} – \mathbf{d} , Deposition morphology of lithium on Ni/LiF nanocomposite substrate in LDME electrolyte (\mathbf{a}), All F electrolyte (\mathbf{b}), DOLDME electrolyte (\mathbf{c}) and F-Free electrolyte (\mathbf{d}). Current density, 0.5 mA cm $^{-2}$ (top), 10 mA cm $^{-2}$ (bottom); capacity, 0.1 mAh cm $^{-2}$. \mathbf{e} – \mathbf{h} , Current–size dependence of lithium

nucleation in LDME electrolyte (\mathbf{e}), All F electrolyte (\mathbf{f}), DOLDME electrolyte (\mathbf{g}) and F-Free electrolyte (\mathbf{h}). For \mathbf{e} - \mathbf{h} , dots with error bars are experimental results, and dashed lines and legend show the fitting results. For \mathbf{e} - \mathbf{h} , statistics are derived from the measurement of four different spots on the substrate (n = 4). Data are presented as mean \pm s.d.

Figure 2a and Supplementary Fig. 20 show the morphology of lithium deposited under different applied current densities on the Ni/LiF nanocomposite substrate in the LDME electrolyte. The size of lithium particles deposited under different current densities is measured and plotted in Fig. 2e. Application of a linear fit to the $\log(i_{\rm applied})$ versus $\log(r)$ plot yields a slope of -3.90 ± 0.41 . Supplementary Table 2 shows the models that have been customized by considering the different θ correlations (Supplementary Figs. 14–17). If we assume that in the case of the Ni/LiF substrate and the LDME electrolyte, the dominant factors for lithium nucleation are nuclei formation and interfacial lithium transport, the model can be simplified to:

$$i_{\text{applied}} = \frac{\frac{2\gamma V_{\text{Li}}}{F}}{\beta \frac{3.94RT}{D_2 C_2 F^2} r^{3.94}}$$
(9)

This will yield a $\log(i_{\text{applied}})$ versus $\log(r)$ slope of -3.94, agreeing perfectly with the experimental observation. No other combinations of the terms would yield a value for the slope that is in such close agreement. Thus, we have identified the limiting processes in this case to be

lithium nuclei formation and interfacial lithium transport, which are both controlled by the nature of the substrate.

Figure 2b-d and Supplementary Fig. 20 show morphologies of lithium nucleation in other electrolytes, which are expected to have similar bulk Li⁺ transport rates, but with very different SEI lithium transport properties. Comparisons between the models and the experimental results (Supplementary Table 2) indicate two distinct categories: substrate controlled and SEI controlled. For lithium nucleation in LDME and All F electrolytes, the nucleation process is limited by lithium nuclei formation and interfacial lithium transport, making the nucleation process substrate controlled, whereas for DOLDME and F-Free electrolytes, lithium nucleation is limited by the SEI through-plane lithium transport and the charge-transfer reaction, which are controlled by the chemistry $of the \, SEI \, (SEI \, controlled). \, These \, insights \, help \, us \, explain \, the \, observations$ in Fig. 1. If the SEI is not limiting lithium transport and the charge-transfer reaction, lithium nucleation tends to be dominated by the properties of the substrate (LDME and All F cases). However, in electrolytes that show a slow SEI through-plane lithium transport and slow charge-transfer kinetics, the nucleation process becomes SEI controlled, which is independent of the substrate chemistry (DOLDME and F-Free cases).

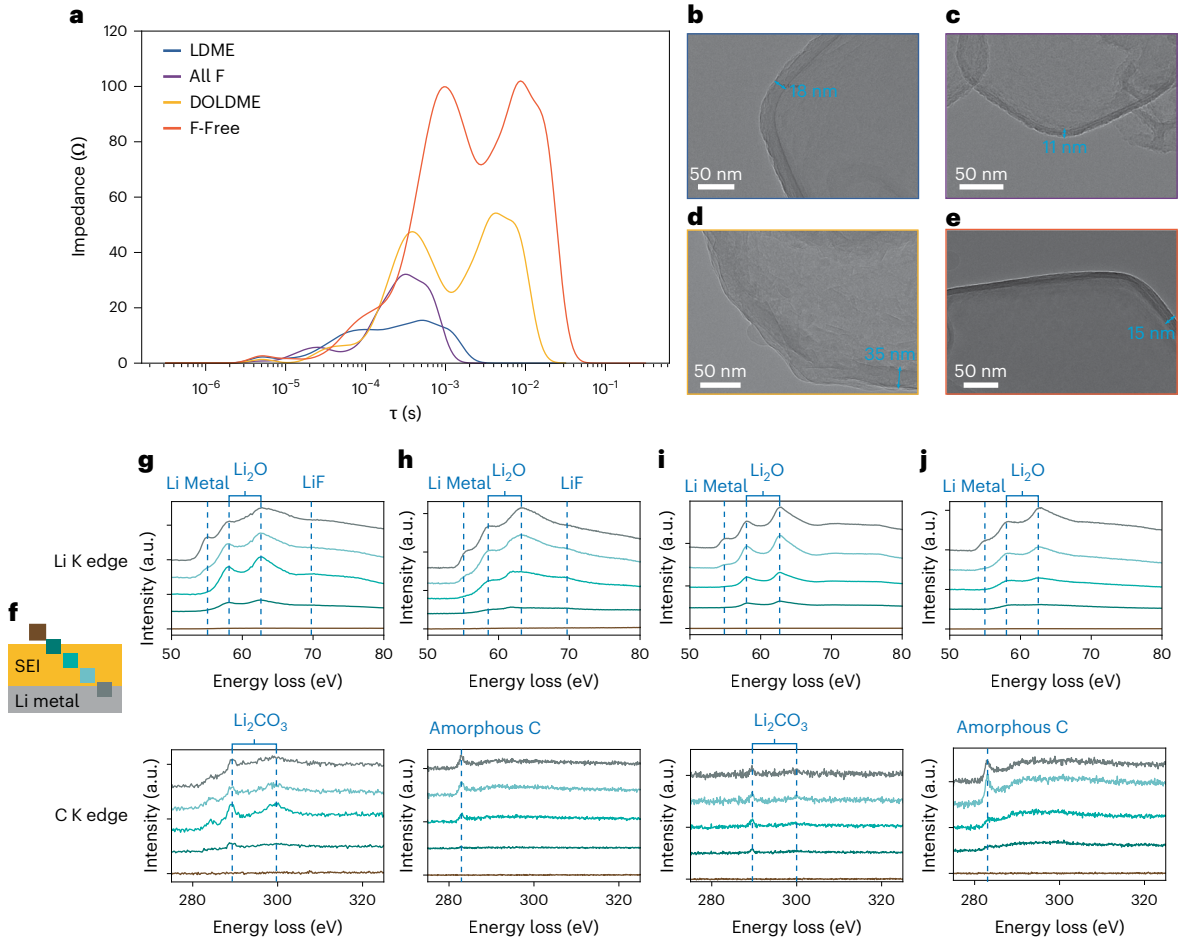


Fig. 3 | Characterization of electrolyte-lithium metal interface (SEI). a, The distribution of relaxation times profile from EIS measurements of lithiated Ni/LiF substrate after SEI formation in four electrolytes. \mathbf{b} - \mathbf{e} , Cryo-TEM images of deposited lithium on a NiF₂-coated TEM grid in LDME electrolyte (\mathbf{b}), All F electrolyte (\mathbf{c}), DOLDME electrolyte (\mathbf{d}) and F-Free electrolyte (\mathbf{e}). Deposition

capacity, 0.2 mAh cm⁻². \mathbf{f} , Illustration showing the beam positions regarding the SEI and lithium metal. \mathbf{g} - \mathbf{j} , Cryo-STEM-EELS spectrum of lithium–electrolyte interface (SEI) in LDME electrolyte (\mathbf{g}), All F electrolyte (\mathbf{h}), DOLDME electrolyte (\mathbf{i}) and F-Free electrolyte (\mathbf{j}).

Correlating SEI chemistry and structure with its role in regulating lithium nucleation

We next examine which chemical and structural features of the SEI make it the limiting factor for lithium nucleation. Electrochemical impedance spectroscopy (EIS) is used to study the lithium transport and charge-transfer kinetics in different electrolytes. Supplementary Fig. 21 shows the EIS spectra after the substrate is biased at 0.01 V for 24 h. This state represents the substrate before lithium nucleation but after the SEI is formed. These data are then fitted via the distribution of relaxation times model, in which the cell impedance is represented as a continuum of repeating parallel resistor-capacitor circuits which enables kinetic analysis of the cell as a function of the time constant^{41,42}. As shown in Fig. 3a, two distinct peaks are identified with two different time constants. The peak with the lower time constant is associated with lithium transport in the SEI, while the peak with the higher time constant is correlated with charge transfer⁴³. Compared to the LDME and All F electrolytes, the impedance for SEI lithium transport and charge transfer are much higher for the DOLDME and F-Free electrolytes. This observation is consistent with the lithium nucleation mechanism discovered from the models in the previous section. Noticeably, the impedance for the F-Free electrolyte is the highest, consistent with the large polarization (Supplementary Fig. 11) and the small nuclei sizes (Fig. 1d).

Cryogenic TEM (cryo-TEM) (Fig. 3b-e) and scanning transmission electron microscopy (STEM) with electron energy loss spectroscopy

(EELS) (Fig. 3f-i) under cryogenic conditions are used to investigate the morphology and chemistry of the SEI formed in different electrolytes. As shown in Fig. 3b-e, clear interface regions can be observed on the surfaces of the deposited lithium metal. The SEI in DOLDME (Fig. 3d) is much thicker (~35 nm) than those formed in the other electrolytes (~15 nm). In the STEM-EELS analysis, five spots at different depths within the SEI are selected to examine the depth profile of the SEI composition. As shown in Fig. 3g and Supplementary Fig. 22, the SEI formed in LDME is dominated by inorganic species such as Li₂O, LiF and Li₂CO₃. In contrast, the SEI formed in the F-free electrolyte (Fig. 3j) only shows a single peak at lower energy (283-284 eV) in the carbon K edge spectra, without any signs of Li₂CO₃ formation. The low-energy peak is associated with amorphous carbon materials⁴⁴, an indication of an organic-rich SEI. Meanwhile, Supplementary Fig. 22 also shows the presence of a Li-B-O compound in the SEI from F-Free electrolyte, indicating the reaction between LiBOB salt and lithium metal. For the SEI formed in the All-F electrolyte, although the carbon K edge spectra (Fig. 3h) also show signals of organic components, the lithium K edge and fluorine K edge spectra (Supplementary Fig. 22) display strong LiF signals. This is consistent with a previous report³⁹ demonstrating that the All-F electrolyte-derived SEI is rich in LiF. For the SEI formed in the DOLDME electrolyte, Li₂O and Li₂CO₃ signals are observed on the lithium K edge spectra (Fig. 3i) and oxygen K edge spectra (Supplementary Fig. 22). However, only a very weak Li₂CO₃ peak is seen on the carbon

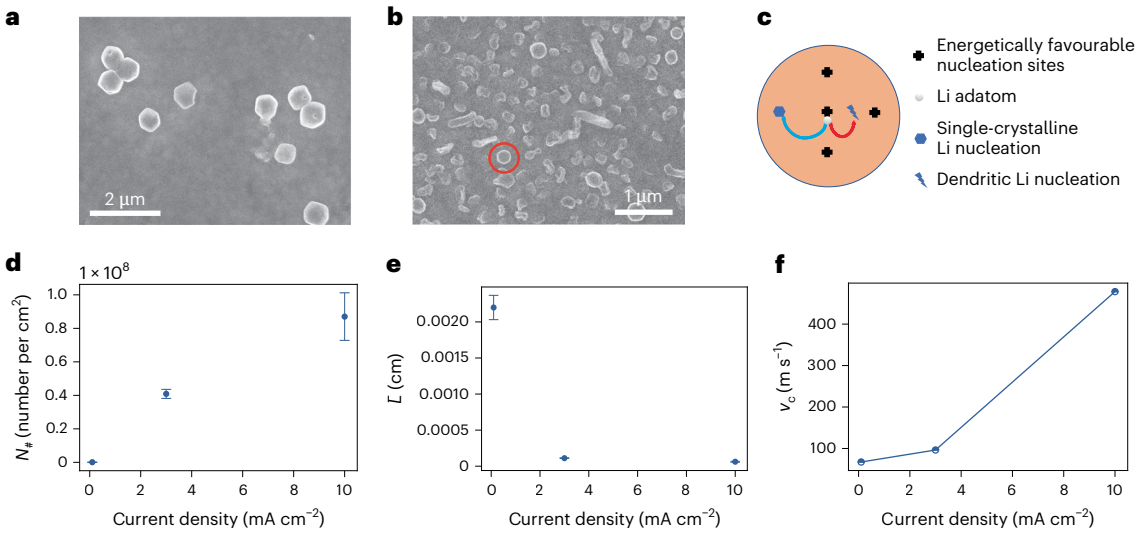


Fig. 4 | **Quantifying the role of the substrate. a**, Lithium nucleation morphology on Ni/LiF nanocomposite substrate. Current density, 3 mA cm $^{-2}$; capacity, 0.01 mAh cm $^{-2}$. **b**, Lithium nucleation morphology on copper substrate. Current density, 3 mA cm $^{-2}$; capacity, 0.01 mAh cm $^{-2}$, in LDME electrolyte. **c**, Schematic illustration of the criteria for substrate-regulated uniform lithium nucleation.

d, Energetically favourable nucleation site density versus applied current density. **e**, Average nucleation site interdistance versus applied current density. **f**, Critical lithium adatom velocity versus applied current density. For **d** and **e**, statistics are derived from the measurement of three different spots on the substrate (n = 3). Data are presented as mean \pm s.d.

K edge spectra (Fig. 3i). We think this inconsistency is due to damage of the sample from the beam during scanning. The morphology of the SEI after the EELS scan (Supplementary Fig. 23) indeed indicates severe damage caused by the beam. Such extreme sensitivity to a low-dose electron beam is an indication of an SEI of an organic-rich nature. A previous report 45 has also concluded that the SEI formed in the DOLDME electrolyte is composed of $\rm Li_2O$ and $\rm Li_2CO_3$ components distributed inside a continuous organic polymer matrix. The EELS-based analysis of SEI chemistry is further corroborated by the X-ray photoelectron spectroscopy (XPS) results shown in Supplementary Fig. 24. The SEIs from DOLDME and F-Free electrolytes have a higher carbon content, indicating their organic-rich nature. Detailed XPS data (Supplementary Fig. 25) also show the inorganic-rich or LiF-rich nature of SEIs formed in LDME and All-F electrolytes.

By summarizing impedance measurements, and the morphological and chemical characterization results, we can correlate lithium nucleation modes with the physical properties of different SEIs. With a thin and inorganic/LiF-rich SEI⁴⁶, the lithium transport through the SEI and the charge-transfer process tend to be fast^{47,48}, which leads to a substrate-controlled mode of lithium nucleation (LDME and All F cases). On the contrary, a thick and/or organic-rich SEI appears to impede lithium transport through the SEI and slow down the charge-transfer reaction, thus limiting the nucleation process and leading to the SEI-controlled mode of lithium nucleation (DOLDME and F-Free cases).

Quantifying the role of substrates in lithium nucleation

We have thus established the criteria for the electrolyte and SEI that enable substrate-controlled lithium nucleation. As shown in Fig. 1a–d, initial lithium nucleation appears dendritic on copper and forms uniform seeds on the Ni/LiF nanocomposite substrate. Uniform single-crystalline lithium nucleation is known to help reduce the porosity of deposited lithium and improve the cycling stability of lithium metal batteries²⁵. Next, we seek to quantify the intrinsic attributes of the substrate that would enable such uniform lithium nucleation.

Figure 4 shows the very early-stage lithium nucleation morphology on the Ni/LiF nanocomposite substrate (Fig. 4a) and on the copper substrate (Fig. 4b). The deposition capacity is 0.01 mAh cm $^{-2}$. Compared with lithium nucleation on copper, lithium nuclei on Ni/LiF

substrate have a much lower number density and a larger internuclei distance, indicating a faster lithium surface migration rate on the Ni/LiF substrate 23,40 . Moreover, lithium nucleation on the Ni/LiF substrate forms uniform rhombic dodecahedra of -0.6 μ m in size. Interestingly, during this early-stage deposition, single-crystalline nuclei are also found on copper, although much smaller in size (-0.2 μ m, such as the one circled in red in Fig. 4b). A similar substrate-controlled lithium nucleation morphology is also detected for the All-F electrolyte system (Supplementary Fig. 26). To explain this substrate effect on lithium nucleation, we propose the following hypothesis:

- For all substrates, there are always low-energy nucleation sites that allow for energetically stable single-crystalline lithium nucleation.
- 2. The key criteria to enable globally uniform single-crystalline lithium nucleation is that lithium adatoms must diffuse fast enough to reach stable nucleation sites instead of forming new nuclei.

We formulate a model to quantify the rates of lithium adatoms moving between the two closest stable nucleation sites versus the rate of critical nuclei formation. We assume that the low-energy nucleation sites are uniformly distributed, with a number density of $N_{\#}$ (number per cm²) and an average intersite distance of \bar{L} (cm). From classical nucleation theory (CNT), the critical nuclei size, $r_{\rm c}$ (cm), is correlated with overpotential, η (V) by:

$$r_{\rm c} = \frac{2\gamma V}{Fn} \tag{10}$$

where γ is the interfacial energy (J cm⁻²) and V is the molar volume of lithium (cm³ mol⁻¹). The time for critical nuclei formation, t_c (s), under a constant-current deposition condition, is expressed by:

$$t_{\rm c} = \frac{Q_{\rm c}}{i_{\#}} = \frac{64\pi\gamma^3 V^2}{3F^2} * \frac{N_{\#}}{i_{\rm applied} * \eta^3}$$
(11)

where Q_c (mAh) is the capacity of one critical nucleus and $i_\#$ (A) is the current on each nucleus. A detailed derivation of Q_c and $i_\#$ can be found in Supplementary Section 5.

As illustrated in Fig. 4c, to enable uniform single-crystalline lithium nucleation, the lithium adatom should be able to diffuse between two

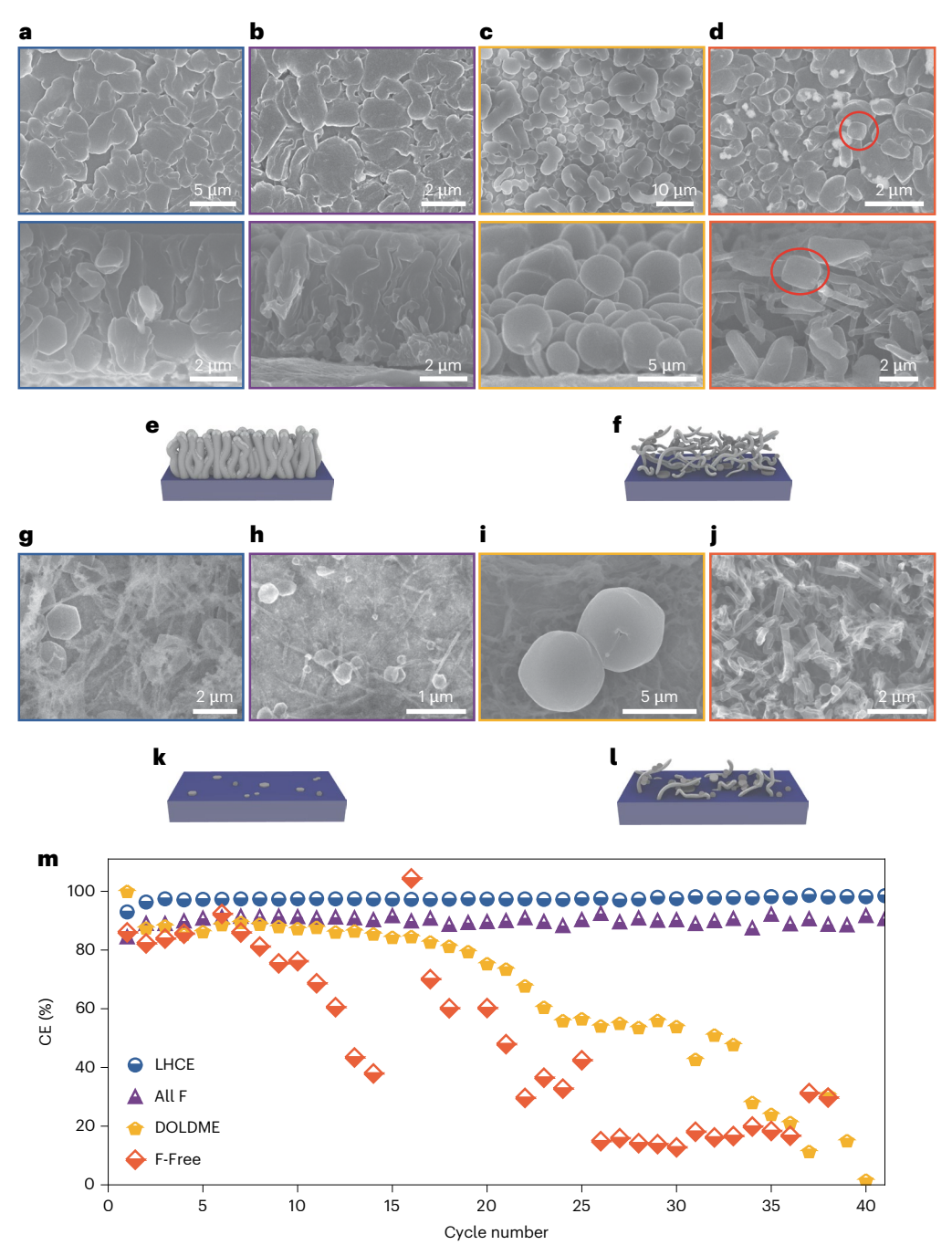


Fig. 5 | Impact of nucleation behaviour on lithium growth mode and cycling stability. \mathbf{a} – \mathbf{d} , Morphology of lithium deposited on Ni/LiF nanocomposite in LDME electrolyte (\mathbf{a}), All F electrolyte (\mathbf{b}), DOLDME electrolyte (\mathbf{c}) and F-Free electrolyte (\mathbf{d}). Current density, 3 mA cm $^{-2}$; capacity, 1 mAh cm $^{-2}$. Top row, top-down view; bottom row, cross-sectional view. Red circles highlight the newly nucleated lithium particles on predeposited lithium surface. \mathbf{e} , Schematic of deposited lithium in nucleation-extrusion-styled growth mode. \mathbf{f} , Schematic of deposited lithium in nucleation-driven multilayer growth mode.

 $g{\text -}j$, Morphology of stripped Ni/LiF nanocomposite after deposition and stripping in LDME electrolyte (g), All F electrolyte (h), DOLDME electrolyte (i) and F-Free electrolyte (j). Current density, 3 mA cm $^{-2}$; capacity, 1 mAh cm $^{-2}$. k, Schematic of the stripped substrate after nucleation-extrusion-styled growth. l, Schematic of the stripped substrate after nucleation-driven multilayer growth. m, Coulombic efficiency (CE) test of lithium versus Ni/LiF cells with different electrolytes. Current density, 3 mA cm $^{-2}$; capacity, 1 mAh cm $^{-2}$.

nucleation sites before the formation of critical nuclei. Thus, the minimum (critical) velocity for lithium adatoms, ν_c (cm s⁻¹), is expressed by:

$$v_{\rm c} = \frac{\bar{L}}{t_{\rm c}} = \frac{3F^2}{64\pi \gamma^3 V^2} * \frac{i_{\rm applied} * \eta^3}{N_\#} * \bar{L}$$
 (12)

The model can be tested experimentally. For lithium nucleation on copper under different current densities, the actual $N_{\#}$ and \bar{L} values

can be estimated through SEM image analysis (Fig. 4b and Supplementary Fig. 27). As shown in Fig. 4d,e, with the increase in applied current density, the nuclei density increases due to a greater overpotential (driving force), which also leads to the reduction of the average internuclei distance. Figure 4f shows the critical lithium adatom velocity (v_c) on copper as a function of applied current density. Due to the significantly accelerated speed of lithium critical nuclei formation, a greater lithium adatom critical velocity is required for single-crystalline

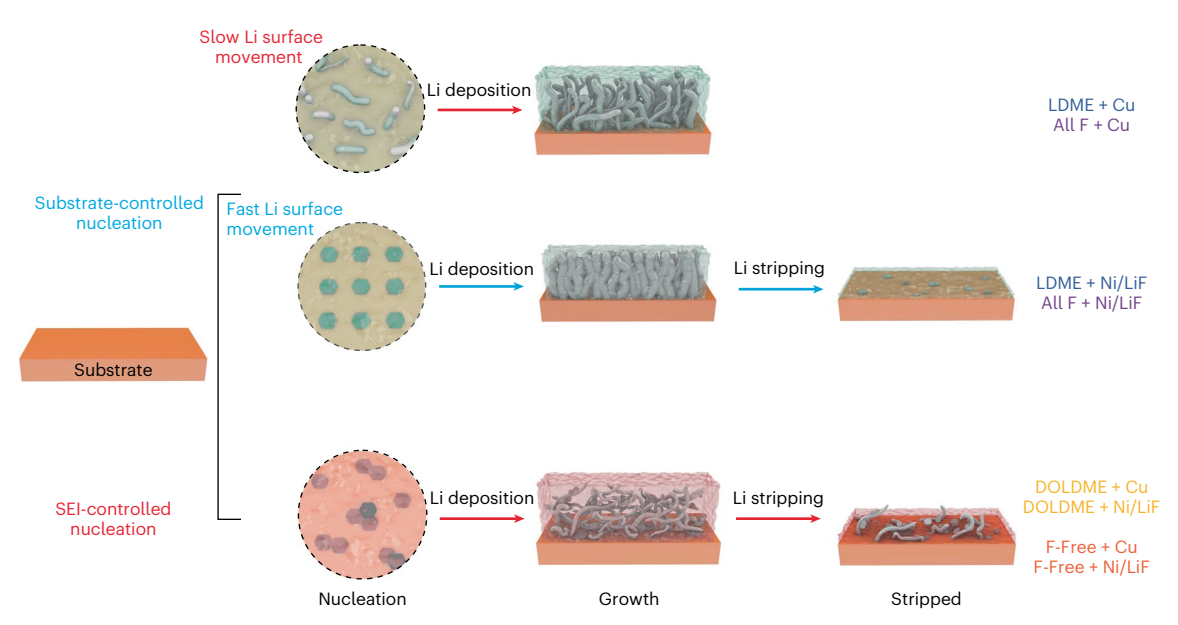


Fig. 6 | Schematic illustration of the impact of two interfaces on the lithium nucleation, growth and stripping process. The illustration highlights the critical influence of both the lithium/electrolyte and lithium/substrate interfaces on lithium nucleation, which dictates the subsequent lithium growth modes and its stripping reversibility.

lithium nucleation under higher current densities. The lithium adatom velocity on a given substrate is an intrinsic property. Results from Fig. 4f indicate that for the copper substrate, lithium nucleation under a lower current density has a greater chance of forming single-crystalline nuclei. This is indeed confirmed experimentally. Under a very low current density (0.1 mA cm⁻²), lithium nucleation on copper forms uniform single crystals (Supplementary Fig. 28a). When the current density is increased (3 mA cm⁻², 10 mA cm⁻²), the nucleation morphology transforms from single crystals to dendrites (Supplementary Fig. 28b,c). This analysis shows that lithium adatom surface movement needs to outpace the critical nuclei formation to generate uniform single-crystalline lithium nucleation. In this regard, a substrate with a high adatom velocity, and uniform and high-density low-energy nucleation sites is highly desirable.

Impact of lithium nucleation on cycling stability

We next examine how the modes of lithium nucleation and the SEI properties dictate the subsequent lithium growth and plating/stripping reversibility. The SEM images in Supplementary Figs. 29-32 and Fig. 5a-d show the morphological evolution of deposited lithium at different capacities in all four electrolytes. With the Ni/LiF nanocomposite substrate, lithium deposition in all electrolytes starts from uniform nucleation (Fig. 1). In the LDME and All F electrolytes, lithium whiskers start to extrude from the lithium nuclei (Supplementary Figs. 29 and 30), thicken and merge (Supplementary Figs. 31 and 32), eventually forming a dense layer (Fig. 5a,b). In contrast, in the DOLDME and F-Free electrolyte, lithium extrusion is rarely observed. Instead, a new layer of lithium crystals nucleates on top of the previously deposited lithium, leading to a layer-by-layer nucleation style growth. We note that for the F-Free electrolyte, the lithium particles are highly non-uniform in size and shape, along with poor connectivity. Lithium nucleation on the previously deposited lithium surface can be clearly observed in the F-Free system over the course of lithium growth, even after 1 mAh cm⁻² of deposition (Fig. 5d, examples of lithium nucleation on the predeposited lithium are highlighted by red circles).

We think that such distinct lithium growth styles are the results of different nucleation modes. For substrate-controlled nucleation (with non-limiting SEI), lithium nucleation only takes place on the original substrate, followed by lithium extrusion, and thickening and merging

of whiskers, eventually forming a well-connected structure (Fig. 5e). On the contrary, with SEI-controlled nucleation, the organic-rich SEI hinders the lithium transport and charge-transfer reaction, thus encouraging new lithium nuclei formation on the previously deposited lithium Such substrate-independent nucleation leads to a layer-by-layer lithium deposition (Fig. 5f). The nucleation-driven multilayer growth mode results in point contact between different layers, which creates structural weak points during subsequent stripping. To better illustrate the two different growth styles, we performed lithium deposition in a pressure-free cell. As shown in Supplementary Figs. 33 and 34, in the absence of pressure, lithium deposition with a non-limiting SEI still forms a continuous structure (Supplementary Fig. 33), whereas layer-by-layer growth is clearly observed in the system with a limiting SEI (Supplementary Fig. 34).

During the subsequent stripping process, the robust, wellconnected structure (formed in non-limiting SEI systems) allows for the reversible removal of deposited lithium, leaving behind only a small number of single crystals from the initial nucleation layer (Fig. 5g,h,k). In contrast, stripping of lithium from the nucleation-driven multilayer growth mode (in limiting SEI systems) is much less reversible, with more 'dead lithium' left due to the loss of contact between layers (Fig. 5i, j, l). Such a difference is even more pronounced after repeated cycling (Supplementary Fig. 35). Supplementary Fig. 36 shows that for the four electrolyte systems considered in this study, the ageing effect from the corrosion reaction between electrolyte and deposited lithium is negligible within the time scale of our study. The differences in morphological evolution translate into reversibility and stability differences during long-term cycling (Fig. 5m and Supplementary Fig. 37). The nucleation-extrusion-styled growth leads to much more reversible and stable cycling than the layer-by-layer growth. Generally, lithium deposition morphology has been categorized as 'planar' or 'dendritic', with the former implying stable, high-efficiency cycling. We show here that the connectivity between particles is critical. Such connectivity is directly related to the underlying nucleation mechanism and is a better indicator of cycling efficiency and stability.

While the earlier discussion focused on the effect of the SEI chemistry on high-capacity lithium cycling for a Ni/LiF substrate, the effect of the substrate for a desired electrolyte is also profound as has been demonstrated previously²⁵. For example, Supplementary Fig. 38

compares the top-down and cross-sectional SEM images for copper and Ni/LiF substrates while operating in an LDME electrolyte. For a deposition capacity of 3 mAh cm $^{-2}$, the lithium thickness on Ni/LiF is 17.7 μ m, about 60% of the 30.1 μ m shown by the copper control. The top-down morphology is noticeably more dendritic in the case of copper. Furthermore, the Ni/LiF substrate shows much improved plating/stripping reversibility and stability (Supplementary Fig. 39) under a current density of 3 mA cm $^{-2}$ and a capacity of 3 mAh cm $^{-2}$.

A framework to describe lithium nucleation and growth

We present in Fig. 6 a framework to describe the lithium nucleation and growth process. In electrolytes that produce an organic-rich SEI (for example, DOLDME and F-Free electrolytes), lithium nucleation is limited by lithium transport through the SEI and the charge-transfer kinetics (SEI-controlled nucleation), which makes the nucleation process independent of the substrate. Under such a mode, further deposition of lithium features a nucleation-driven multilayer growth. Due to the weak connection between particles, lithium metal electrodes in this system are prone to dead lithium formation upon stripping, which translates to poor lithium plating/stripping reversibility and stability. However, in electrolytes that produce inorganic/LiF-rich SEIs (for example, LDME and All F electrolytes), the nucleation process is limited by lithium transport on the substrate surface and the formation of lithium nuclei (substrate-controlled nucleation). A substrate (for example, Ni/LiF nanocomposite substrate) with dense, uniform nucleation sites and fast lithium adatom transport on its surface enables highly uniform nucleation. In such combined system, the lithium growth after nucleation primarily involves extrusion from the pre-existing lithium nuclei, which produces lithium particles with robust electronic connectivity. The electrode has a much lower tendency for isolated, dead lithium formation and is more reversible and stable for cycling.

In summary, we have used physics-based models to uncover the effects of lithium-substrate and lithium-SEI interfaces on lithium nucleation. Additionally, contrary to the usual treatment that categorizes lithium growth morphology by particle shape (for example, dendritic versus spherical), we elucidated the effects of nucleation modes on lithium plating/stripping reversibility and found that the continuous nucleation-induced lithium growth mode is detrimental to the cyclability of lithium metal anodes. Based on our analysis⁵⁰, coupling a well-designed substrate (for example, LiF-rich substrate with uniform low-energy nucleation sites or very clean lithium) and an electrolyte that derives inorganic-rich SEI (LHCE electrolytes, highly fluorinated electrolyte, etc.) would promote uniform lithium nucleation and continuous lithium growth, thus significantly improving the reversibility and stability of the lithium metal anode. We hope that this study not only deepens our understanding of lithium nucleation processes, but also links lithium nucleation to the subsequent growth process and opens a new window to understand and optimize lithium metal anode cycling stability.

Online content

Any methods, additional references, Nature Portfolio reporting summaries, source data, extended data, supplementary information, acknowledgements, peer review information; details of author contributions and competing interests; and statements of data and code availability are available at https://doi.org/10.1038/s41557-025-01911-y.

References

- Liu, J. et al. Pathways for practical high-energy long-cycling lithium metal batteries. Nat. Energy 4, 180–186 (2019).
- Cheng, X.-B., Zhang, R., Zhao, C.-Z. & Zhang, Q. Toward safe lithium metal anode in rechargeable batteries: a review. *Chem. Rev.* 117, 10403–10473 (2017).
- Lin, D., Liu, Y. & Cui, Y. Reviving the lithium metal anode for high-energy batteries. Nat. Nanotechnol. 12, 194–206 (2017).

- Bai, P., Li, J., R. Brushett, F. & Bazant, Z. M. Transition of lithium growth mechanisms in liquid electrolytes. *Energy Environ. Sci.* 9, 3221–3229 (2016).
- Zhang, W. et al. Recovery of isolated lithium through discharged state calendar ageing. *Nature* 626, 306–312 (2024).
- 6. Thirumalraj, B. et al. Nucleation and growth mechanism of lithium metal electroplating. *J. Am. Chem.* Soc. **141**, 18612–18623 (2019).
- Pei, A., Zheng, G., Shi, F., Li, Y. & Cui, Y. Nanoscale nucleation and growth of electrodeposited lithium metal. *Nano Lett.* 17, 1132–1139 (2017).
- Yan, K. et al. Temperature-dependent nucleation and growth of dendrite-free lithium metal anodes. *Angew. Chem. Int. Ed.* 131, 11486–11490 (2019).
- Guan, X. et al. Controlling nucleation in lithium metal anodes. Small 14, 1801423 (2018).
- Chen, X.-R., Zhao, B.-C., Yan, C. & Zhang, Q. Review on Li deposition in working batteries: from nucleation to early growth. *Adv. Mater.* 33, 2004128 (2021).
- Yan, C. et al. Nucleation and growth mechanism of anion-derived solid electrolyte interphase in rechargeable batteries. *Angew. Chem. Int. Ed.* 133, 8602–8606 (2021).
- 12. Li, N. et al. Normalized lithium growth from the nucleation stage for dendrite-free lithium metal anodes. *Angew. Chem. Int. Ed.* **131**, 18414–18419 (2019).
- Fan, Y. et al. Altering polythiophene derivative substrates to explore the mechanism of heterogeneous lithium nucleation for dendrite-free lithium metal anodes. J. Energy Chem. 59, 63–68 (2021).
- Xu, Y. et al. Promoting mechanistic understanding of lithium deposition and solid-electrolyte interphase (SEI) formation using advanced characterization and simulation methods: recent progress, limitations, and future perspectives. Adv. Energy Mater. 12, 2200398 (2022).
- Yan, K. et al. Selective deposition and stable encapsulation of lithium through heterogeneous seeded growth. *Nat. Energy* 1, 16010 (2016).
- Fang, Y., Zhang, S. L., Wu, Z.-P. & Luan, D. A highly stable lithium metal anode enabled by Ag nanoparticle-embedded nitrogen-doped carbon macroporous fibers. Sci. Adv. 7, eabq3626 (2021).
- Li, S.-Q. et al. A dendrite-free lithium-metal anode enabled by designed ultrathin MgF₂ nanosheets encapsulated inside nitrogen-doped graphene-like hollow nanospheres. Adv. Mater. 34, 2201801 (2022).
- Huang, G. et al. Lithiophilic 3D nanoporous nitrogen-doped graphene for dendrite-free and ultrahigh-rate lithium-metal anodes. Adv. Mater. 31, 1805334 (2019).
- Zhang, R. et al. Lithiophilic sites in doped graphene guide uniform lithium nucleation for dendrite-free lithium metal anodes.
 Angew. Chem. Int. Ed. 129, 7872–7876 (2017).
- He, J. & Manthiram, A. 3D CoSe@C aerogel as a host for dendrite-free lithium-metal anode and efficient sulfur cathode in Li–S full cells. Adv. Energy Mater. 10, 2002654 (2020).
- Chi, S.-S. et al. Lithiophilic Zn sites in porous CuZn alloy induced uniform Li nucleation and dendrite-free Li metal deposition. Nano Lett. 20, 2724–2732 (2020).
- 22. Park, S., Jin, H.-J. & Yun, Y. S. Advances in the design of 3D-structured electrode materials for lithium-metal anodes. *Adv. Mater.* **32**, 2002193 (2020).
- 23. Sun, J. et al. Lithium deposition mechanism on Si and Cu substrates in the carbonate electrolyte. *Energy Environ. Sci.* https://doi.org/10.1039/D2EE01833K (2022).
- Ozhabes, Y., Gunceler, D. & Arias, T. A. Stability and surface diffusion at lithium-electrolyte interphases with connections to dendrite suppression. Preprint at https://arxiv.org/ abs/1504.05799v1 (2015).

- Wu, Z. et al. Growing single-crystalline seeds on lithiophobic substrates to enable fast-charging lithium-metal batteries.
 Nat. Energy 8, 340–350 (2023).
- Boyle, D. T. et al. Resolving current-dependent regimes of electroplating mechanisms for fast charging lithium metal anodes. Nano Lett. 22, 8224–8232 (2022).
- Yuan, X., Liu, B., Mecklenburg, M. & Li, Y. Ultrafast deposition of faceted lithium polyhedra by outpacing SEI formation. *Nature* 620, 86–91 (2023).
- Biswal, P., Stalin, S., Kludze, A., Choudhury, S. & Archer, L. A. Nucleation and early stage growth of Li electrodeposits. Nano Lett. 19, 8191–8200 (2019).
- Shi, Y. et al. Interfacial evolution of lithium dendrites and their solid electrolyte interphase shells of quasi-solid-state lithium-metal batteries. *Angew. Chem. Int. Ed.* 59, 18120–18125 (2020).
- Fan, X. et al. Fluorinated solid electrolyte interphase enables highly reversible solid-state Li metal battery. Sci. Adv. 4, eaau9245 (2018).
- 31. Liu, Y. et al. Self-assembled monolayers direct a LiF-rich interphase toward long-life lithium metal batteries. *Science* https://doi.org/10.1126/science.abn1818 (2022).
- 32. Zhang, Q. et al. Synergetic effects of inorganic components in solid electrolyte interphase on high cycle efficiency of lithium ion batteries. *Nano Lett.* **16**, 2011–2016 (2016).
- 33. Yan, C. et al. Lithium nitrate solvation chemistry in carbonate electrolyte sustains high-voltage lithium metal batteries. *Angew. Chem. Int. Ed.* **57**, 14055–14059 (2018).
- 34. Liu, Y. et al. Electro-chemo-mechanical modeling of artificial solid electrolyte interphase to enable uniform electrodeposition of lithium metal anodes. *Adv. Energy Mater.* **12**, 2103589 (2022).
- Shen, X. et al. The failure of solid electrolyte interphase on Li metal anode: structural uniformity or mechanical strength? Adv. Energy Mater. 10, 1903645 (2020).
- Li, N.-W. et al. A flexible solid electrolyte interphase layer for long-life lithium metal anodes. *Angew. Chem. Int. Ed.* 130, 1521–1525 (2018).
- Yoon, I., Jurng, S., Abraham, D. P., Lucht, B. L. & Guduru, P. R. Measurement of mechanical and fracture properties of solid electrolyte interphase on lithium metal anodes in lithium ion batteries. *Energy Storage Mater.* 25, 296–304 (2020).
- Liu, H. et al. Ultrahigh coulombic efficiency electrolyte enables Li||SPAN batteries with superior cycling performance. Mater. Today 42, 17–28 (2021).

- Fan, X. et al. Non-flammable electrolyte enables Li-metal batteries with aggressive cathode chemistries. *Nat. Nanotechnol.* 13, 715–722 (2018).
- 40. Biswal, P. et al. The early-stage growth and reversibility of Li electrodeposition in Br-rich electrolytes. *Proc. Natl Acad. Sci. USA* **118**, e2012071118 (2021).
- 41. Danzer, M. A. Generalized distribution of relaxation times analysis for the characterization of impedance spectra. *Batteries* **5**, 53 (2019).
- 42. Holoubek, J. et al. Toward a quantitative interfacial description of solvation for Li metal battery operation under extreme conditions. *Proc. Natl Acad. Sci. USA* **120**, e2310714120 (2023).
- Zhang, S. S., Xu, K. & Jow, T. R. Electrochemical impedance study on the low temperature of Li-ion batteries. *Electrochim. Acta* 49, 1057–1061 (2004).
- 44. Liao, Y. Practical electron microscopy and database. https://www.globalsino.com/EM/ (2006).
- 45. Han, B. et al. Cryo-electron tomography of highly deformable and adherent solid-electrolyte interphase exoskeleton in Li-metal batteries with ether-based electrolyte. *Adv. Mater.* **34**, 2108252 (2022).
- 46. Fan, X. et al. All-temperature batteries enabled by fluorinated electrolytes with non-polar solvents. *Nat. Energy* **4**, 882–890 (2019).
- Lu, Y., Tu, Z. & Archer, L. A. Stable lithium electrodeposition in liquid and nanoporous solid electrolytes. *Nat. Mater.* 13, 961–969 (2014).
- 48. Ma, X.-X. et al. The origin of fast lithium-ion transport in the inorganic solid electrolyte interphase on lithium metal anodes. Small Structures 3, 2200071 (2022).
- 49. Dong, K. et al. Unravelling the mechanism of lithium nucleation and growth and the interaction with the solid electrolyte interface. ACS Energy Lett. **6**, 1719–1728 (2021).
- 50. Hui, Z. Source data NCHEM-24071878B.zip. figshare https://doi.org/10.6084/m9.figshare.29466917.v1 (2025).

Publisher's note Springer Nature remains neutral with regard to jurisdictional claims in published maps and institutional affiliations.

Springer Nature or its licensor (e.g. a society or other partner) holds exclusive rights to this article under a publishing agreement with the author(s) or other rightsholder(s); author self-archiving of the accepted manuscript version of this article is solely governed by the terms of such publishing agreement and applicable law.

© The Author(s), under exclusive licence to Springer Nature Limited 2025

Methods

NiF₂ thin-film deposition

The NiF₂ thin film was prepared by thermal evaporation (Angstrom Engineering Nexdep EB Evaporator) of NiF₂ powder (Sigma-Aldrich) onto copper foil (9 μ m thick), at 20% power for 15 min.

Electrolyte preparation

The LDME electrolyte was prepared by dissolving 2 M LiFSI in DME/BTFE (1:4 w/w). Here, 1 M is defined as 1 M salt dissolved into 1 litre of solvent. LiFSI was purchased from Sigma-Aldrich, DME was purchased from Gotion and BTFE was purchased from Tokyo Chemical Industry (TCI).

The All F electrolyte was prepared by dissolving 1 M LiPF $_6$ in FEC/TTE/FEMC (1:3:1 w/w/w). Lithium hexafluorophosphate (LiPF $_6$) was purchased from Gotion, FEC was purchased from Sigma-Aldrich, and TTE and FEMC were purchased from TCI.

The DOLDME electrolyte was prepared by dissolving 1 M LiTFSI in DOL/DME (1:1 v/v) +1 wt% LiNO $_3$. LiTFSI and DOL were purchased from Gotion. Lithium nitrate (LiNO $_3$) was purchased from Sigma-Aldrich.

The F-free electrolyte was prepared by dissolving 1 M LiBOB in EC/DMC (1:1 v/v). LiBOB) and EC were purchased from Sigma-Aldrich. DMC was purchased from Gotion.

Battery assembly

Coin cells (2016-type) were used for lithium deposition and half-cell testing. Each cell included a 250- μ m lithium chip (12 mm in diameter), a 25- μ m Celgard-2325 separator (19 mm in diameter), a 1-mm spacer (15 mm in diameter), a piece of bare copper or NiF₂-coated copper (16 mm in diameter), and 75 μ l of electrolyte.

Electrochemical testing

Lithium deposition and half-cell tests were conducted on a Neware tester. Cells were first discharged at $100~\mu A~cm^{-2}$ until 0.2~V. An additional 24~h of 0.2~V constant voltage hold was applied in the NiF $_2$ cells to fully lithiate the thin film. With this hold at low voltage, the thin-film NiF $_2$ fully converts to Ni/LiF. Then, the cells were discharged at $100~\mu A~cm^{-2}$ until 0~V. Once 0~V was reached, constant-current discharges with different current densities and deposition time were applied to deposit lithium. Cells for the morphology observations were disassembled after deposition. Cells for the plating/stripping testing were then stripped to 1~V.

SEM

For morphological observations of lithium, cells were disassembled in an argon-filled glovebox. The deposited lithium was washed with the same solvent used in its electrolyte to remove residual electrolyte. The morphologies of the deposited lithium were characterized by SEM (JEOL JSM-7400F field emission scanning electron microscope).

SEM image analysis

ImageJ software was used to extract quantitative information (that is, crystal size and number density) from the SEM images.

Cryo-S/TEM and EELS

Cryo-S/TEM and EELS analyses were conducted using a 300-kV FEI Titan Krios G3 scanning transmission electron microscope (S/TEM) equipped with a Gatan BioContinuum 1067HD energy filter (EF) and post-filter mounted K3 Direct Electron Detector with STEM and EELS support. Sample preparation mirrored the protocols reported in our previous paper²⁵, with lithium electrochemically deposited onto NiF₂-coated TEM grids (with lacey carbon, 300-mesh) in a coin cell. The deposited TEM grids were washed in a glovebox and stored in argon-filled bags. These bags were submerged in liquid nitrogen before the samples were clipped using Thermo Fisher Autogrid c-clips and rings to allow loading using the microscope's autoloader system. All data acquisition was done at 80 K with either an EFTEM fringe-free nanoprobe or in EFSTEM mode.

The energy slit was retracted during the imaging. Low-magnification TEM images accumulated a total dose of approximately $0.1\,e\,\mathring{A}^{-2}$, while high-magnification TEM images had accumulated approximately $40\,e\,\mathring{A}^{-2}$ total dose. All TEM imaging was motion corrected within Gatan Digital Micrograph software and collected in correlated double-sampling mode. EELS experiments acquired data with a 68–135 pA beam current and 0.1 s dwell time per pixel. Aggregating spectra from multiple pixels was used to enhance the signal-to-noise ratios.

XPS

XPS (Physical Electronics, Quantera Scanning XPS Microprobe System) was carried out using an aluminium anode source at 15 kV. Obtained data were calibrated based on a reference C–C bond energy of 284.6 eV and fitted in CasaXPS.

Atomic force microscope

Substrate roughness and electronic conductivity characterization were carried out using a Park NX20 atomic force microscope. The film roughness was measured using an NSC15 probe. Conductive AFM was performed using an ElectriMulti75-G probe, with a bias voltage of $3.0 \, \text{V}$.

Data availability

The data supporting the findings of this study are available within the article and its Supplementary Information. Source data are provided with this paper.

Acknowledgements

The work was supported by the Office of Vehicle Technologies of the US Department of Energy through the Advanced Battery Materials Research (BMR) Program (Battery500 Consortium) under contract number PNNL-595241 (P.L.). Part of the work used the UCSD-MTI Battery Fabrication Facility. We specially acknowledge help from the UCSD cryo-EM centre and from M. Matyszewski with the cryo-S/TEM+EELS characterizations.

Author contributions

Z.H., S.Y. and P.L. conceived the idea. P.L. directed the project. Z.H. developed the quantitative models and performed the electrochemical experiments and SEM characterizations. S.W. performed the XPS characterization. G.H. helped with the graphical representation of data. J.H. helped with model development and data analysis. K.Z. and M.L. helped with the cryo-TEM experiments. Q.M., V.P. and H.L. helped with SEM characterization. S.T. performed the conductive atomic force microscopy characterization. H.L. helped with electrolyte selection and preparation. K.Z., J.N. and J.Z. provided input on data interpretation and manuscription preparation. Z.H., S.Y., G.H., K.Z, J.N. and P.L. co-wrote and revised the paper.

Competing interests

The authors declare no competing interests.

Additional information

Supplementary information The online version contains supplementary material available at https://doi.org/10.1038/s41557-025-01911-y.

 $\label{lem:correspondence} \textbf{Correspondence} \ \textbf{and} \ \textbf{requests} \ \textbf{for materials} \ \textbf{s} \ \textbf{hould} \ \textbf{be} \ \textbf{addressed} \ \textbf{to} \ \textbf{Ping Liu}.$

Peer review information *Nature Chemistry* thanks Tao Gao, Qiang Zhang and the other, anonymous, reviewer(s) for their contribution to the peer review of this work.

Reprints and permissions information is available at www.nature.com/reprints.